Structures 69 (2024) 107392

Contents lists available at ScienceDirect

Structures

journal homepage: www.elsevier.com/locate/structures

Numerical and experimental investigation on angle multiple slit bolted connections for precast wall panels

Bruno Dal Lago *

Department of Theoretical and Applied Sciences, Università degli Studi dell'Insubria, Varese, Italy

ARTICLE INFO

Keywords:
Precast structures
Wall panels
Angle connections
Multiple slit
Bolted joint

ABSTRACT

Flat Multiple Slit Devices (MSDs) have been introduced in steel constructions located in earthquake-prone areas as compact hysteretic dampers connected to braces, and were further proposed to be employed also in other structural typologies, including aligned precast concrete walls. Nevertheless, similar angle connections needed for horizontal joints of orthogonal walls are not tackled in literature. The shape of MSDs, obtained by selective weakening by removing part of the steel area of flat plates, may allow to attain a highly ductile and stable dissipative behaviour, given local plate buckling is avoided, protecting the bolted joints through capacity design. Laser cutting as an alternative to mechanical milling introduces the possibility to easily optimise the shape of the slits in order to attain better performance under laterally imposed cyclic load. This paper analyses the application of right-angle-bent MSDs for the horizontal connection between orthogonal precast walls typical of panel structures with rigid diaphragms. In particular, bolted angle plates with hourglass-shaped multiple slits obtained after laser cutting are investigated numerically via non-linear finite shell elements and experimentally with original cyclic tests. The effect of the aspect ratio of the plate and of the restraint condition, possibly affecting the performance under imposed shear deformation due to the presence of the bent corner, is investigated by parametric analysis. Finally, general design rules and recommendations are presented.

1. Introduction

Added hysteretic damping is among the most popular strategies to enhance the seismic performance of a structural assembly [1–7]. Hysteretic devices typically consume energy through plasticisation of structural steel, which can occur under imposed axial [8], shear [9,10], bending, or torque [11] mechanism, alone or in combination. With reference to the bending flexural mechanism, Added Damping And Stiffess (ADAS) dissipative systems were introduced on the basis of a series of cantilevering triangular steel plates subjected to out-of-plane imposed displacement [2,3,12], where the transverse triangular shape allowed to obtain uniform yielding along the length of the plates, enhancing the deformation capacity of the system subjected to lateral load. More recently, series of elementary beams acting in flexure were obtained within single plates by milling creating multiple slits which, subjected to lateral loading in the plane of the elementary beams, transform the stiff shear mechanism of the initial plate into a more deformable flexural mechanism. This technique also allows to selectively weaken [13] the central portion of the plate with respect to the edges, when provided with either bolted or welded connection with the structural elements, protecting it from a semi-brittle failure by capacity design and transforming it into a ductile mechanism with much higher deformation capacity. Basic devices employ constant profile rectangular beams [14–24]. Plates not carved for the full depth, mixing the shear behaviour of the thin plate thickness left in the centre with the flexural behaviour of the elementary beams, were also recently proposed [25,26]. However, the rectangular shape profile is not optimised, since, when subjected to imposed lateral displacement/loading, it tends to concentrate the higher stress in the elementary beam ends, by forming discrete plastic hinges. As a result of many researchers who tackled the issue of topologic optimisation of the plate experimentally, analytically, and/or numerically, the elementary beam profile (depth distribution) of a hourglass results by imposing a uniform-yielding profile [27–40], when the width is kept constant (the thickness of the plate for multiple slit devices). Such shaping, which allows to enhance the displacement capacity of the elementary beams whilst keeping the same strength of the rectangular-profile elementary beams, can smartly be obtained with modern laser cutting technologies [41]. Similar technologies have also

* Correspondence to: Università degli Studi dell'Insubria, Department of Theoretical and Applied Sciences, Via Dunant 3, 21100 Varese, Italy.
E-mail address: bruno.dallago@uninsubria.it.

https://doi.org/10.1016/j.istruc.2024.107392
Received 12 September 2023; Received in revised form 20 August 2024; Accepted 25 September 2024

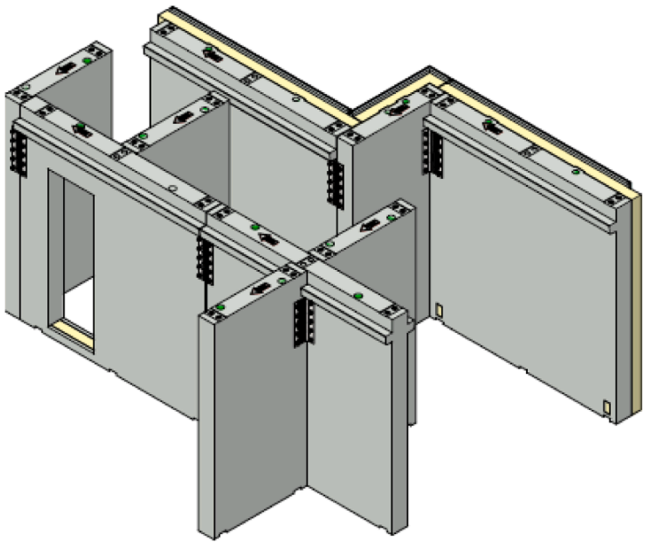

Fig. 1. Typical horizontal joint configurations employing flat and angular multiple slit devices in precast wall panel structures.

been proposed to be carved in non-flat plates or profiles [42–44]. Moreover, some authors proposed to couple the hysteretic yielding behaviour of multiple slit devices with friction, further enhancing the deformation capacity of the device, although typically the two mechanisms need to be carefully calibrated to efficiently work in series [31,45,46]. The use of multiple slit plates was mainly proposed for steel frame structures, both in dissipative braces [47–56], or in frame joints [57–62]. However, they were recently proposed to be used also in between precast concrete elements, either in frame elements [19,63,64] or as horizontal joints of wall structures [31,38,39,65,66], as an alternative mainly to dissipative friction connections [67–69]. The employment of multiple slit devices as ductile connections for mid- and high-rise precast buildings appears to be promising, since they could not only serve as energy dissipation fuses during earthquake events, but they could also serve as ductile connectors able to accommodate relatively large differential instantaneous and creep settlements, replacing typical brittle shear key joints [70] and allowing for controlled mutual deformation capacity between adjacent or transverse walls under thresholded actions. In this context, several horizontal joint configurations can be found in a typical building, some of which can be solved with the use of flat plates, and some of which need to be solved with angular plates, as shown in Fig. 1.

Angular connectors are common in precast structures [71–74]. Despite this, there is no information in the current literature concerning the adaptation of angle plates to multiple slit devices, the influence of the plate bending, and the restraint condition of the bolts in the orthogonal surfaces.

This paper aims at filling this gap by providing a combined experimental and numerical investigation on the influence of plate bending and restraint condition of the bolts over the structural response of angle multiple slit devices, proposing general design rules.

2. Prototypal angle devices

The prototypal angle device proposed is produced starting from a flat steel plate, on which slotted holes and slits are laser cut. After this operation, the plate is fold at right angle in multiple steps using a bending press. The fuse-shape of the slits is optimised for lateral imposed displacement following the indications provided in [31]. By considering a 10 mm thick plate, and keeping the maximum depth over thickness ratio on the safe side not larger than 2, in order to avoid the risk of lateral buckling even at very large deformation, the single elementary beams results having 20 mm of edge depth and a length of 92 mm. In order to account for the laser cutter encumbrance of 1 mm, several elementary beams were placed in a row at an inter-axis of 21 mm (Fig. 2).

The slots have the function to allow the connection of the angle device with the walls through tightened threaded bars accommodating assemblage tolerances. In particular, the prototype of Fig. 2 is conceived to be installed in wall elements produced in horizontal moulds with mechanical positioning of the steel counterplates containing alternatively a passing hole pipe or a superficial pre-installed mechanical coupler, meaning that the accuracy in the vertical position matching of the slots in the connected wall elements can be dealt with mechanical precision. In this case, tolerance in both horizontal directions is provided by the slots. However, possible alternative cases involving non-mechanical insert precision may lead to a different choice, with one row of slots being vertical instead of horizontal. In such a case, as well as whenever the tolerance given by the slot needs to be deactivated after assemblage for the correct kinematics of the connection, the slots can be coupled with welded toothed profiles, over which the threaded bar is tightened against counter-toothed washers [71]. A further alternative to ensure small tolerances in all directions might be provided by employing larger round holes coupled with a planetary slotted washer and friction bolted connection with large pre-stressing. Finally, a possible alternative solution may concern the use of post-installed anchors, which can simplify the wall production by avoiding the positioning of inserts in the wall moulds, but typically provide a lower resistance, and therefore in this case their design shall be carried out with peculiar accuracy, and in general their diameter should result larger than passing threaded bars.

These angle devices can be classified on the basis of repetitive moduli of 6 elementary beams, to which corresponds a slot row. However, due to the deviation of the load in the edge slots in the restrained configuration, as better detailed in the design rule chapter, the edge elementary beams external to the slot axis are 2.5 instead of 3 (Fig. 2). The device shown in Fig. 2 is therefore characterised by 2 moduli.

To be noted that some joints can only be made from one side only (e.g. joint between external walls, as shown in Fig. 1), while some others can be made adopting two plates on different sides of the joint. In the latter case, it can be decided to adopt two connections, or to adopt a single connection on one side only. It is clear that the number of moduli to be designed depends upon this choice, since the two plates on the same joint act in parallel. Obviously, adopting a double plate configuration is suggested, since it allows also to centre the load in the wall element. Adopting a single plate provides an eccentricity with respect to the centre of gravity of the wall which may result in the distribution of secondary moments in the wall elements, which however can be handled within the design of local wall reinforcement.

3. Numerical simulation of the prototypal device

Numerical models were developed with the aim to simulate the structural performance of a single prototypal device. The 3D finite element model has been developed in Straus7 [75] using 3-nodes tetrahedral shell elements, as shown in Fig. 3. A non-structured mesh was automatically generated by the software after calibration of the total number of elements carried out with a sensitivity analysis. About 8000 tetrahedral shell elements were employed, with average size varying from less than 1 mm closer to the edge discontinuities of the laser-cut slits to about 10 mm near the corners of the angle plate. More information about the shape function, element formulation, integration scheme and auto-meshing procedure can be found in the theoretical manual of the software [75]. A bi-linear elastic-hardening stress-strain behaviour of structural steel is implemented in the model (Fig. 4) on the basis of the nominal characteristic strength properties of the steel grade S355 employed, characterised by nominal yielding and ultimate strength of 355 MPa and 510 MPa, respectively [76]. The corresponding strain points were taken as 0.17 % on the basis of an elastic modulus of 210 GPa, and 20.00 % on the basis of typical experimental ultimate

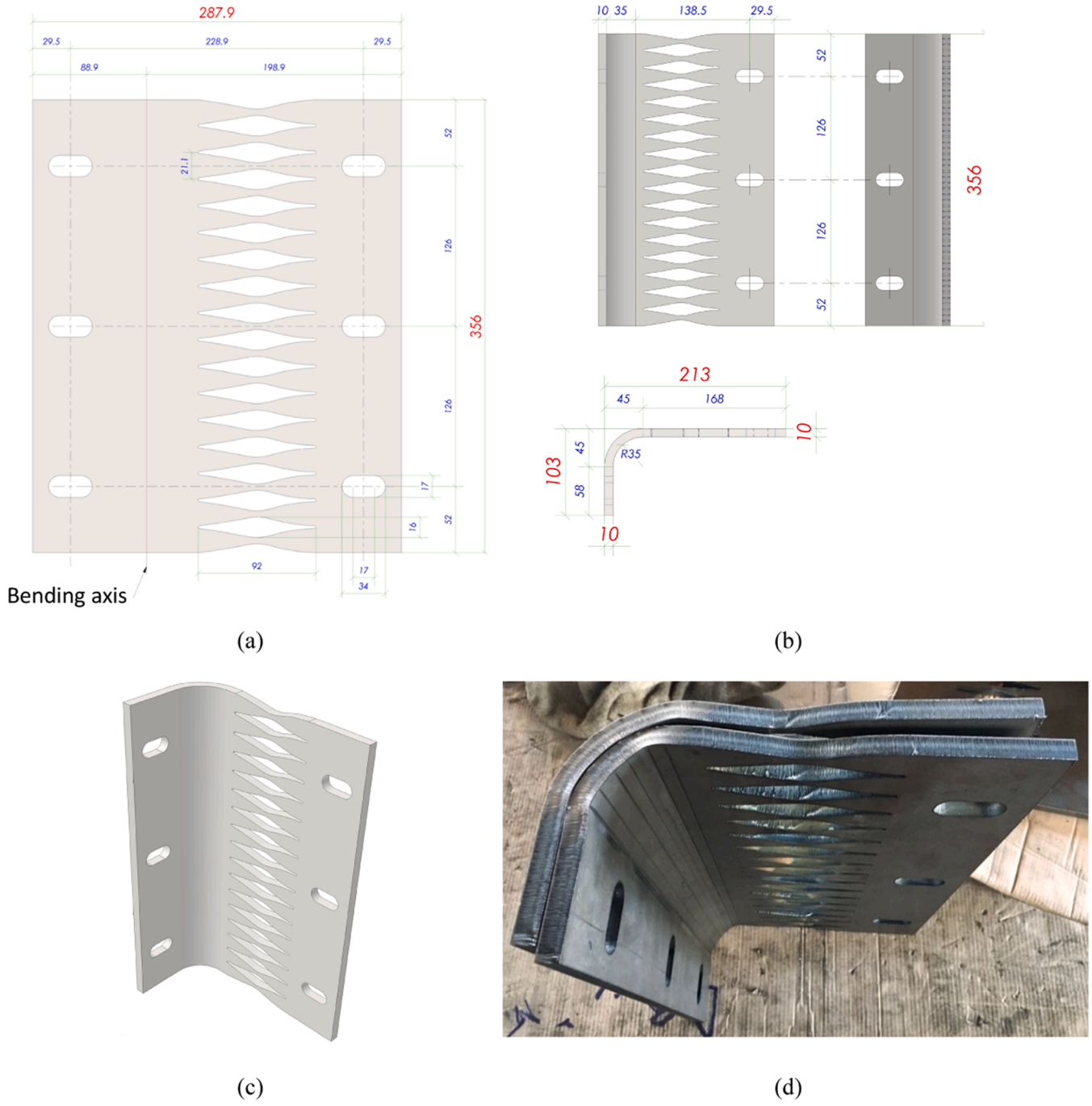

Fig. 2. Specimen proposed to be investigated: (a) geometry of the original flat steel plate to be cut by laser; (b) geometry of the requested bent multiple slit plate; (c) 3D view of the requested multiple slit plate; (d) picture of multiple slit plates after production. Measures in [mm].

strain, respectively. The software does not accept interruptions in the constitutive law, and therefore the hardening branch was left unlimited, with proper individuation of the failure condition done in post-processing by checking the condition that the computed ideal stress does not overcome the ultimate. The geometrical non-linearity is also taken into account by the solver. The solver automatically interpolates or extrapolates the stress values based on the values of strain considering the slope of both linear lines. The Von-Mises yield criterion is used.

Different boundary conditions were considered. The holes of the horizontal short flap of the plate are fully fixed in their centre, and the holes of the vertical flap of the plate are restrained according to two different strategies, schematised in Fig. 5: one named "restrained" simulating the test condition with restraint in the three directions, the alternative one named "unrestrained" investigating the possible degree of freedom of displacement along the direction of the slot.

In both strategies, the in-plane displacement orthogonal to the slit orientation was imposed as the loading condition, simulating a vertical rigid mutual deformation of the wall panels in the context of a building provided with rigid diaphragm, where hence relative horizontal displacements and rotations around the vertical axis are restrained by other mechanical connections (or by a continuous reinforced concrete topping). Moreover, the presence of concrete, physically hampering both flat parts of the plate, was taken into account by imposing stiff-spring compression-only boundary supports in those surfaces. Friction at the interface between plate and concrete was neglected. The threaded bars were not explicitly modelled, and the edge nodes of the slotted

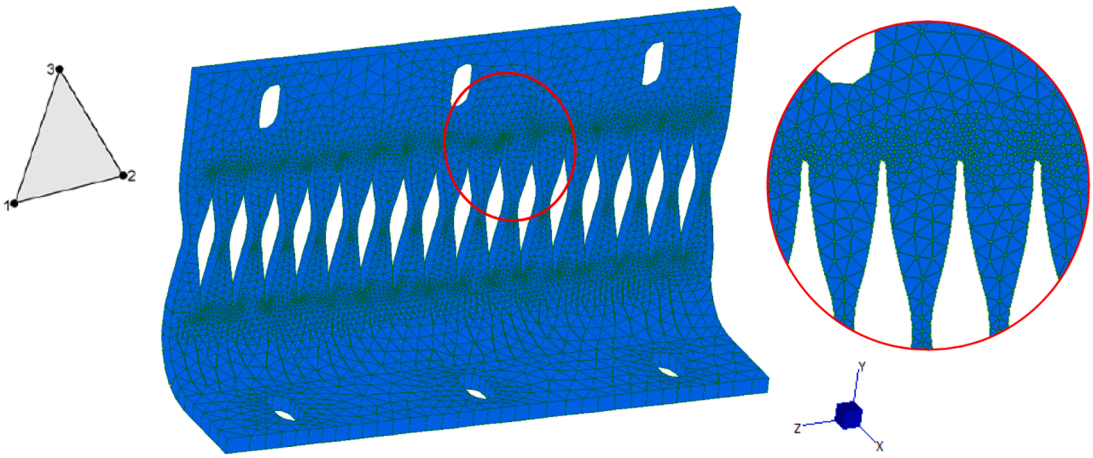

Fig. 3. Numerical model employing 3-nodal tetrahedral shell elements with 2D detail of the non-structured mesh.

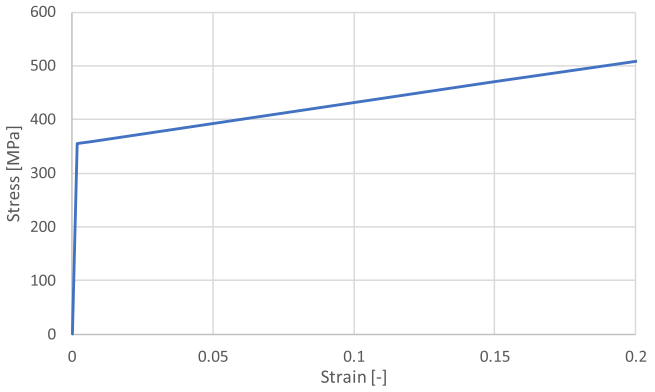

Fig. 4. Bi-linear stress-strain behaviour for steel S355 implemented in the model.

holes were all rigidly connected to each central master node placed in the centre of the slot through rigid links.

To simulate the load in the experiment conditions, a non-linear static analysis including nonlinearity both for geometry and material was carried out by imposing a crescent displacement history applied simultaneously to the three central master nodes of the slots located on the longer flap.

Convergence in the analysis was found at all imposed steps up to the target ultimate displacement of the analysis of 50 mm. It is however reminded that the software considers an unlimited plastic hardening branch of steel, and thus the actual strain of steel obtained as a result of the analysis might be larger than the ultimate.

The pushover curve of the simulation carried out considering the restrained condition (Fig. 6a) shows an onset of yielding occurring at a displacement of 0.8 mm and a load of 81.9 kN.

Von Mises stress contours are shown in Fig. 7 with limits corresponding to the nominal characteristic yield stress (355 MPa) right after yielding, highlighting that yielding first occurs at a section approximately located at 0.40 L, given L is the length of the elementary beams identified by the slits. It is however noted how the perimetral areas of the elementary beams is mostly equally stressed at onset of yielding, highlighting the correct shaping of the beams with the aim of having a diffused yielding along their length. The behaviour at very large displacement tends to further hardening due to 2nd order catenary effect, i.e. the decomposition of the shear force orthogonal to the beam

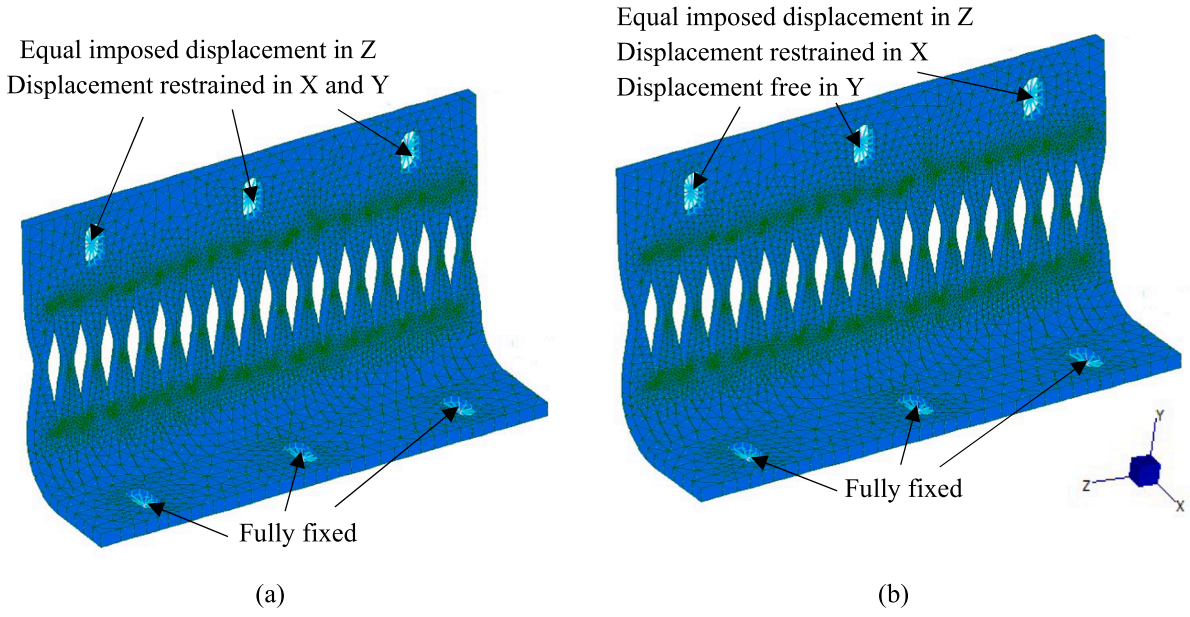

Fig. 5. Node restraints of FE model: (a) restrained condition, (b) unrestrained condition.

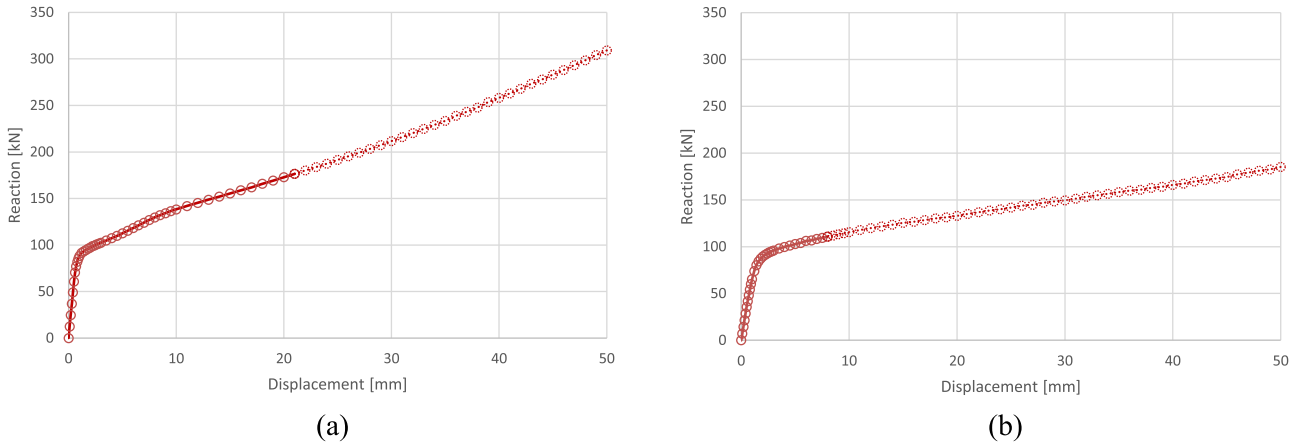

Fig. 6. Pushover curves resulting from the analysis under: (a) restrained condition, (b) unrestrained condition.

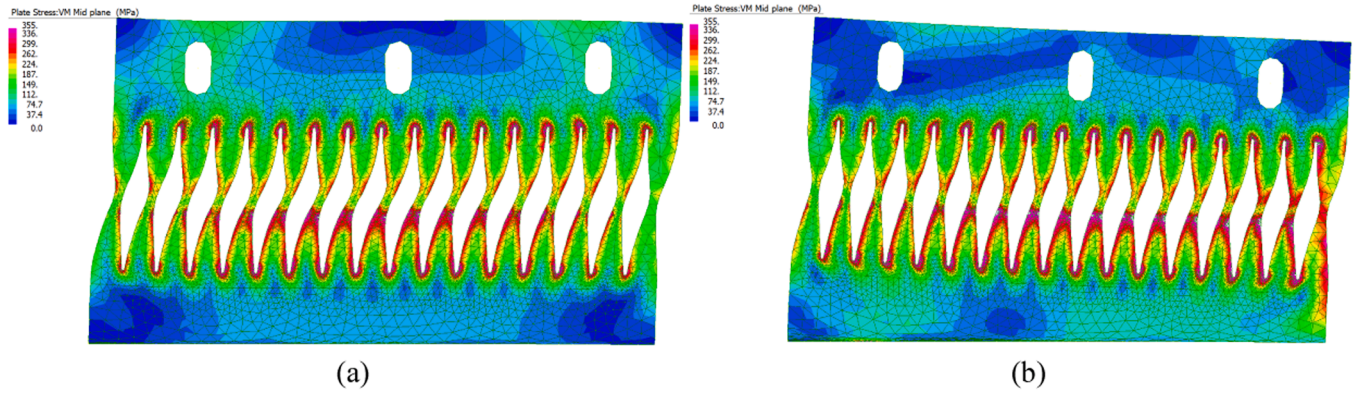

Fig. 7. Deformation and stress state at onset of yielding for the angle plate under: (a) restrained condition – displacement of 0.8 mm, (b) unrestrained condition – displacement of 1.6 mm. Note: displacement magnified with different factor.

axis with the generation of a non-negligible axial component as a function of the inclination angle of the cross-sections around midspan, according to the deformed shape shown in Fig. 7.

Concerning restrained condition, the post-processing underlined that the onset of failure, associated with the ultimate strain, was attained at a displacement of 21.0 mm, associated to a ductility of 21.0 / 0.8 ≈ 26. The elementary beams are highly plasticised, with plastic strains developed along the full depth of most cross-sections. Further plot contours at the bottom of Fig. 8 show the extension of the plasticised region. It is recalled that the condition of ultimate strain was attained very locally in a single finite element of the mesh, which may be deemed to be a conservative assumption. The results of the model obtained removing the displacement constraint in the direction parallel to the slotted holes located in the larger flap of the plate (unrestrained condition – Fig. 6b) show an onset of yielding occurring at a displacement of 1.6 mm at a load of 84.2 kN. Much larger deformability than the one associated to yielding in the restrained condition is noted, although the load is similar. Again, yielding first occurs at a section approximately located at 0.40 L, given L is the length of the elementary beams identified by the slits, and the perimetral areas of the elementary beams is mostly equally stressed at onset of yielding, highlighting the correct shaping of the beams with the aim of having a diffused yielding. However, the displaced shape is obviously influenced by the different restraint condition, and it is clear that strain is not uniformly distributed among all elementary beams, being the ones towards the compressed side (right side of the figure) progressively more stressed.

Concerning unrestrained condition, the post-processing underlined that the onset of failure, associated with the ultimate strain, was attained at a displacement of 8.0 mm, associated to a ductility of 8.0 / 1.6 = 5, much lower with respect to the restrained condition. The stress distribution shows a concentration of plastic stress in the edge beams, due to the additional axial stress caused by the unrestrained boundary condition. In particular, the compressed elementary beam appears to be the critical, due to the contribution of 2nd order effects caused by the compression, as clearly noticeable in Fig. 8b by the deformation of the central part of the slit as well as by the extension of the plasticised region. The lateral view of the displaced shape of the plate shows that more severe out-of-plane deformation and distortion around the bent part of the plate occurred with respect to the restrained condition, where the higher absolute displacement obtained was associated to the much larger ultimate displacement. The out-of-plane deformation of the plate contributed in modifying the stress distribution on the elementary beams. Again, it is recalled that the condition of ultimate strain was attained very locally in a single finite element of the mesh.

4. Experimental testing

Two experimental cyclic tests were performed at the LPMSC laboratory of Politecnico of Milano on the considered joint simulating a T-shaped joint between two orthogonal precast concrete walls. For each specimen, two prototypal MSD angle plates were bolted to solid concrete blocks as shown in Fig. 9, where the specimen is shown in the test position, overturned by 90° with respect to the reference real joint. The concrete blocks have dimensions of 60x60x25 cm and are made with concrete class C45/55 (nominal characteristic cylindric compressive strength of 45 MPa). They are reinforced with standard cages made of 8

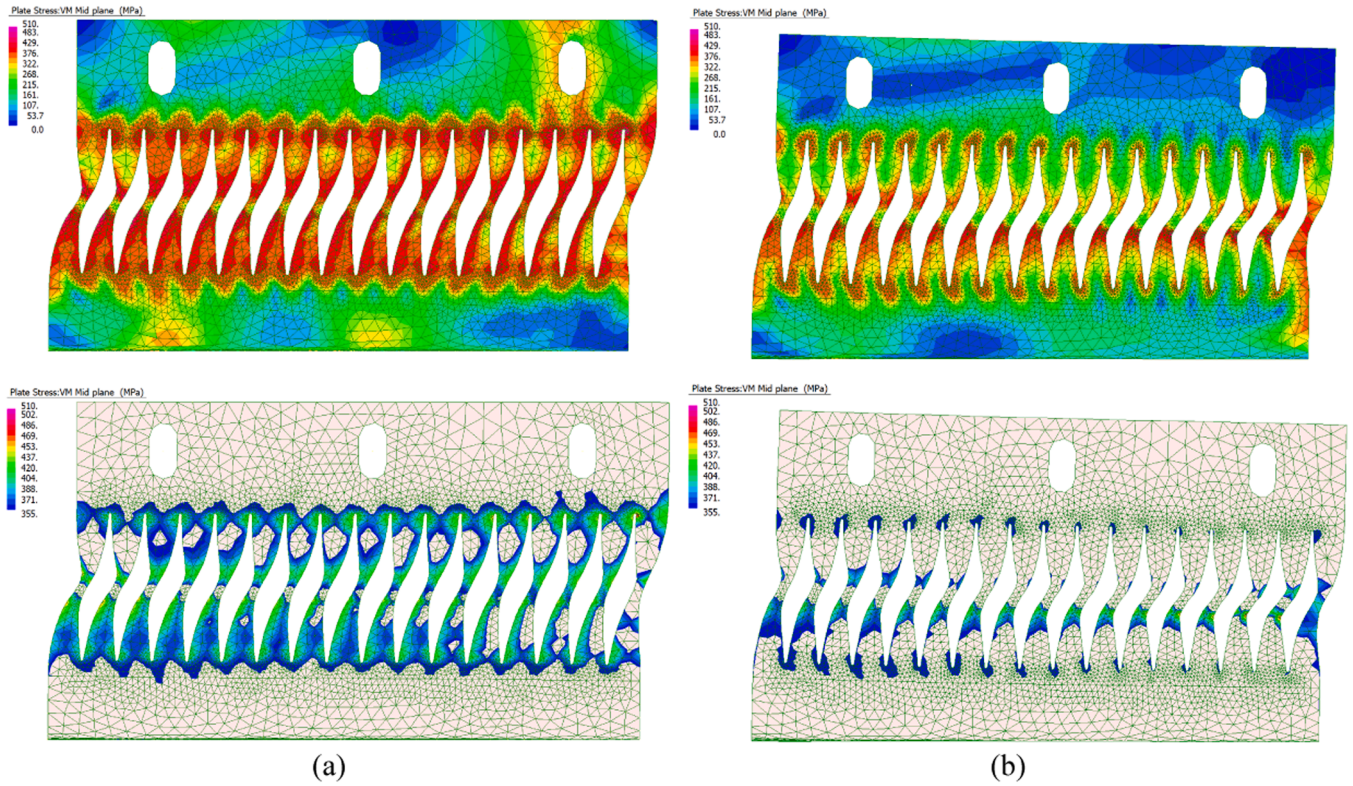

Fig. 8. Deformation and stress state at onset of failure and extension of the plasticised regions for the angle plate under: (a) restrained condition – displ. 21 mm, (b) unrestrained condition – displ. 8 mm. Note: displacement magnified with different factor.

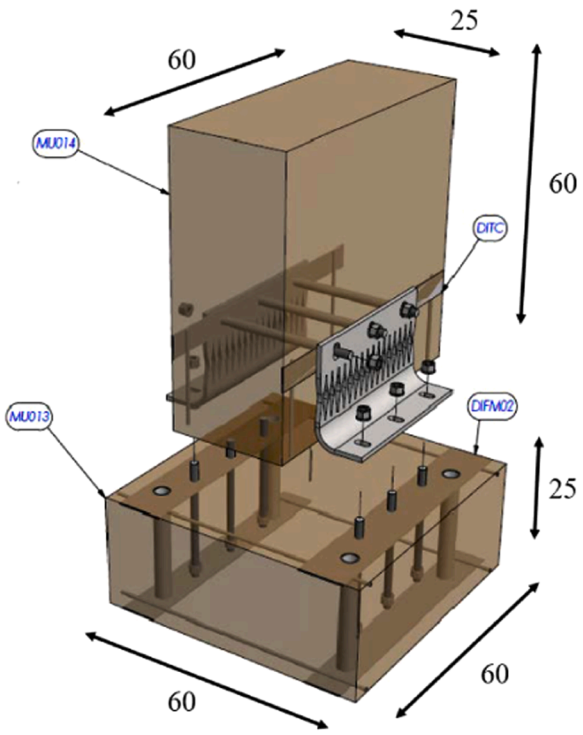

Fig. 9. 3D drawing of the assembling procedure of the specimen subjected to test (measures in [cm]).

Φ12 rebars (one top and one bottom layer in the direction of the reference walls) confined by 8 Φ8 closed stirrups. All reinforcement is made by ribbed bars with steel grade B450C (nominal characteristic yield strength of 450 MPa). It is to be pointed out that the MSD angle plates where originally conceived to be tested in unrestrained condition. However, after the numerical simulations were carried out and analysed, this configuration was questioned, and the plate was transformed into restrained condition by drilling directly in the original Φ17 slotted holes of the slit flaps and in the concrete block larger round holes able to accommodate M24 threaded bars, thus restraining the ability of the plate to move along the direction of these slotted holes (vertical in the test position). The designed M16 threaded bars protruding from the bottom concrete block were left as originally designed and constructed. All bolted connections were strongly tightened manually without employing a dynamometric wrench.

The test setup is shown in Fig. 10. The lower concrete block was fixed to the strong floor of the laboratory by means of vertical M24 threaded bars of steel grade 8.8 passing through the holes left in the lower block by means of plastic pipes in production. The horizontal displacement of the lower block is prevented by a system consisting of plate and counter plate bolted to the strong floor and connected to each other by four additional M24 threaded bars.

A predetermined displacement history was applied to the upper block by means of a hydraulic jack with capacity of 1000 kN anchored to an external strong steel angle fixed to the strong floor. Since the displacement is applied in both push and pull directions, the flat metal plates pinned to the jack is also connected to a strong counterplate by additional four M24 threaded bars. In order to carry out a test under pure shear, avoiding applying external flexure on the plate, simulating typical walls very stiff in flexure, a vertical constraint system was assembled. It consisted in two solid steel prisms placed over the top block, connected each other by means of M24 threaded bars in horizontal and connected to the strong lab floor through the same M24 bars connecting the lower block. In order to avoid lateral displacement of the prisms, both of them are braced by diagonal ties connected to the strong floor. Possible frictional contributions between the steel prisms and the concrete block were minimised by placing Teflon (PTFE) stiff thick

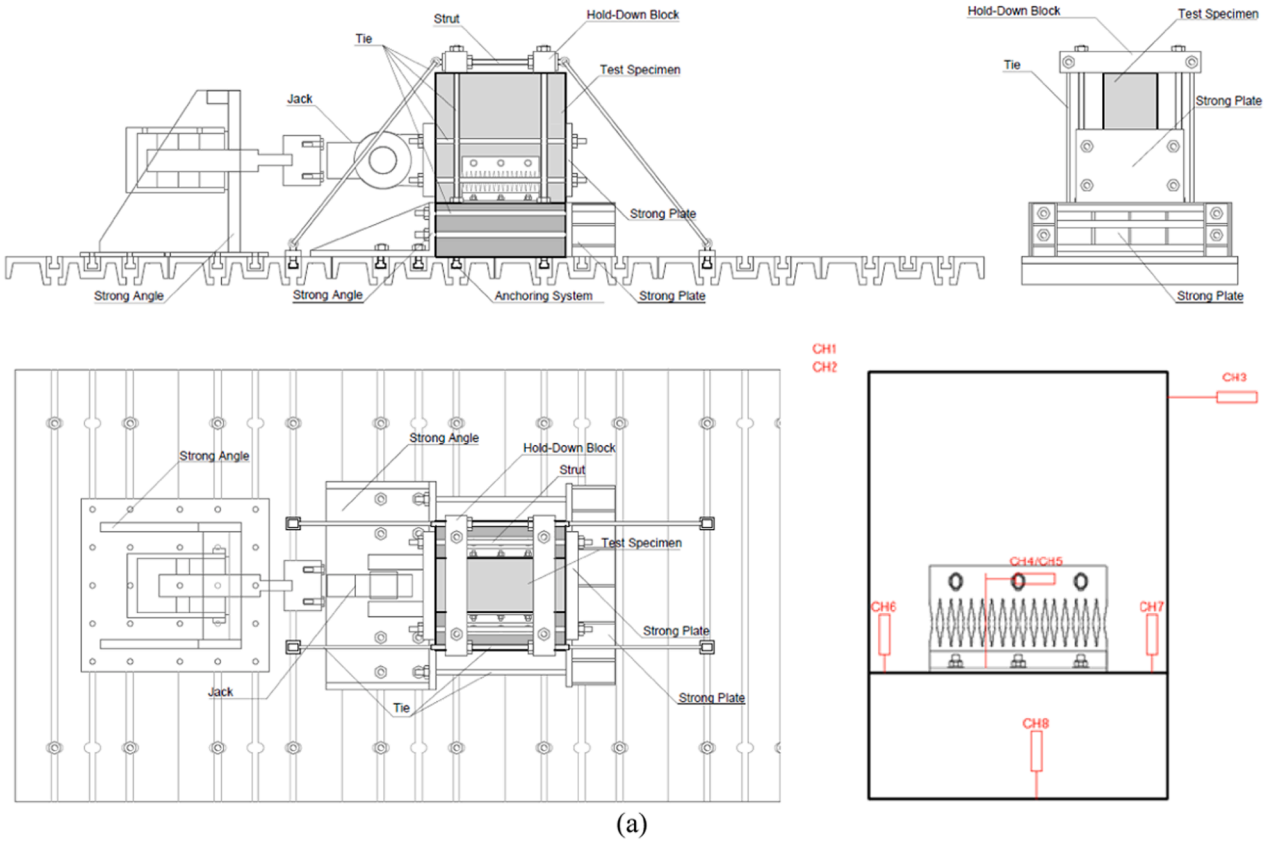

(a)

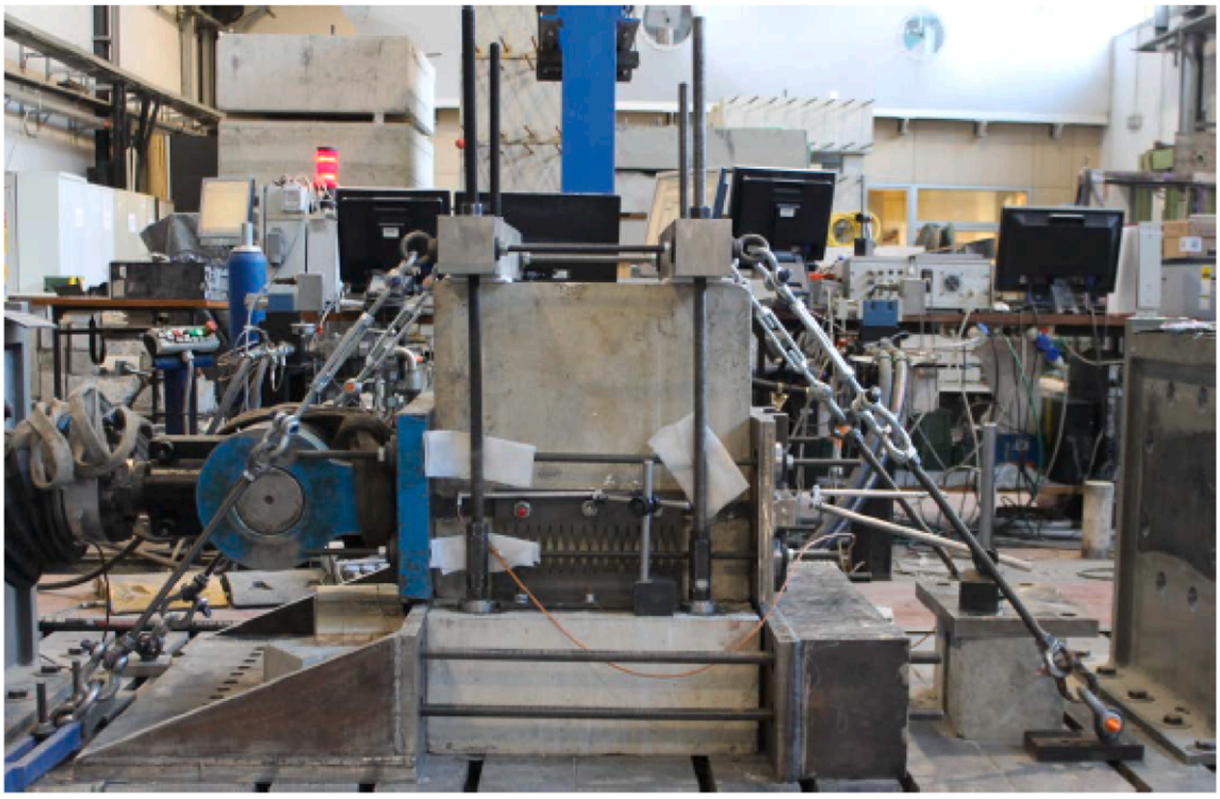

(b)

Fig. 10. Test setup: (a) drawing and instrumentation scheme, (b) picture.

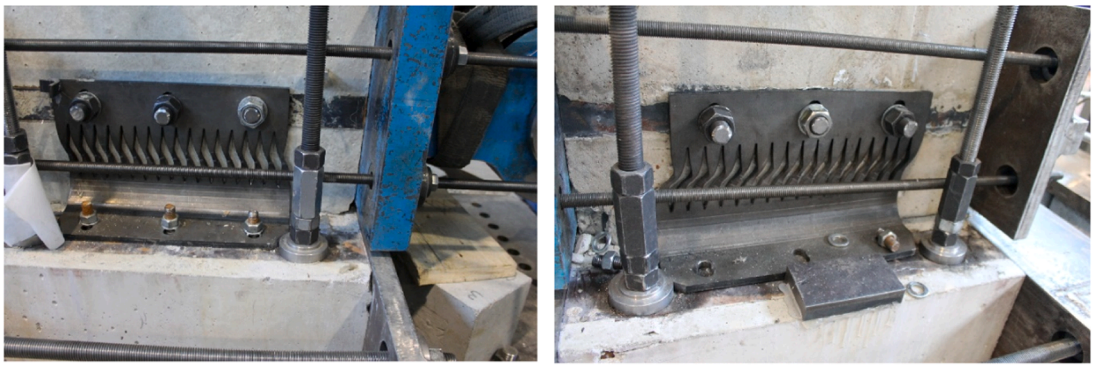

Fig. 11. Specimen at the end of: (a) test 1, (b) test 2.

blocks at the interface. Thin Teflon sheets were also interposed in between close horizontal and vertical threaded bars.

The instrumentation scheme for both tests is schematically showed in Fig. 10a. The loading jack was provided with the control displacement transducer (CH1) and a load cell (CH2). The device CH3, a displacement transducer with stroke of ± 50 mm placed on the block opposite side of the loading jack in axis with it, provides the reference displacement of the overall system. the instrument CH4 measured the difference between the bottom and the top of the metal plate, while the device CH5 measured the difference in displacements between the lower block and the upper part of the plate. The relative vertical displacement between upper and lower block were measured by CH6 and CH7. The further vertical displacement transducer CH8 was installed between the lower concrete block and the lab strong floor to measure possible uplift of the specimen. Each instrument was accurately calibrated before installation over the specimens.

The test protocol employed was in terms of imposed displacement at the reference instrument CH3 based on the general formula shown in Eq. 1, with R repetitions of a displacement amplitude d evaluated as the product of the initial displacement C times a constant A at the n-th power, where n is the number of cycle groups. This protocol of general application (without need to define any yielding or ultimate threshold), was extensively employed by many researchers, as described in [77], and it follows the typical assumption that many small-displacement

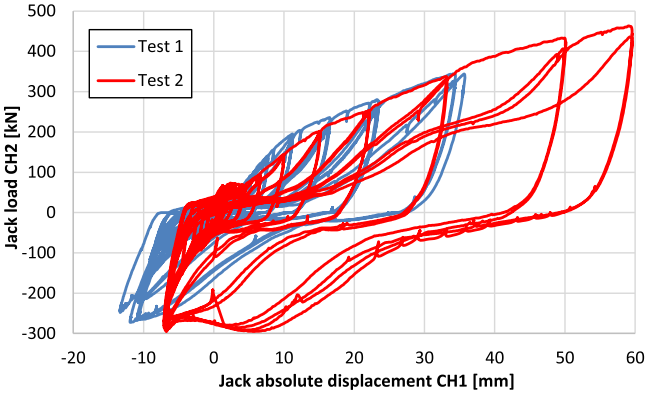

(a)

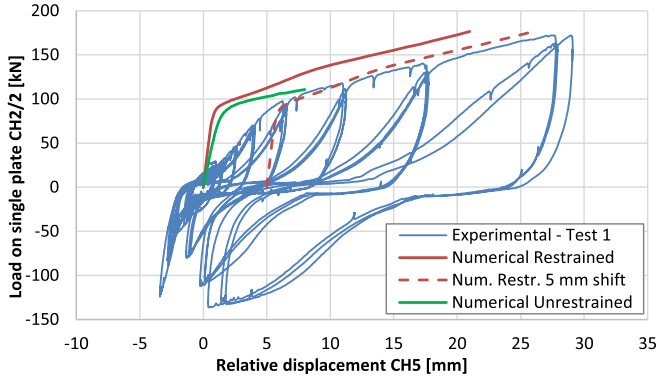

(b)

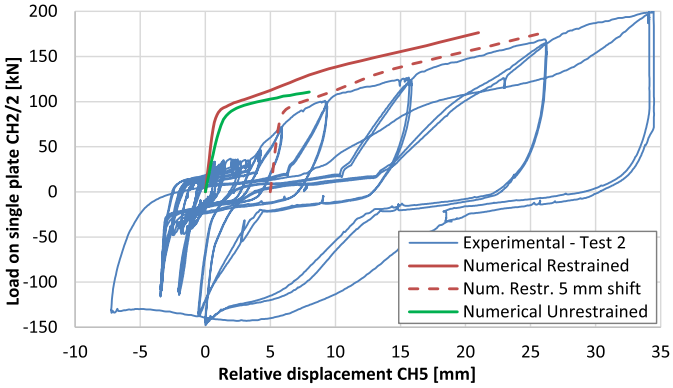

(c)

Fig. 12. Results. (a) Test with absolute jack instruments, (b) Test and simulation with relative displacement - test 1, (c) Test and simulation with relative displacement - test 2.

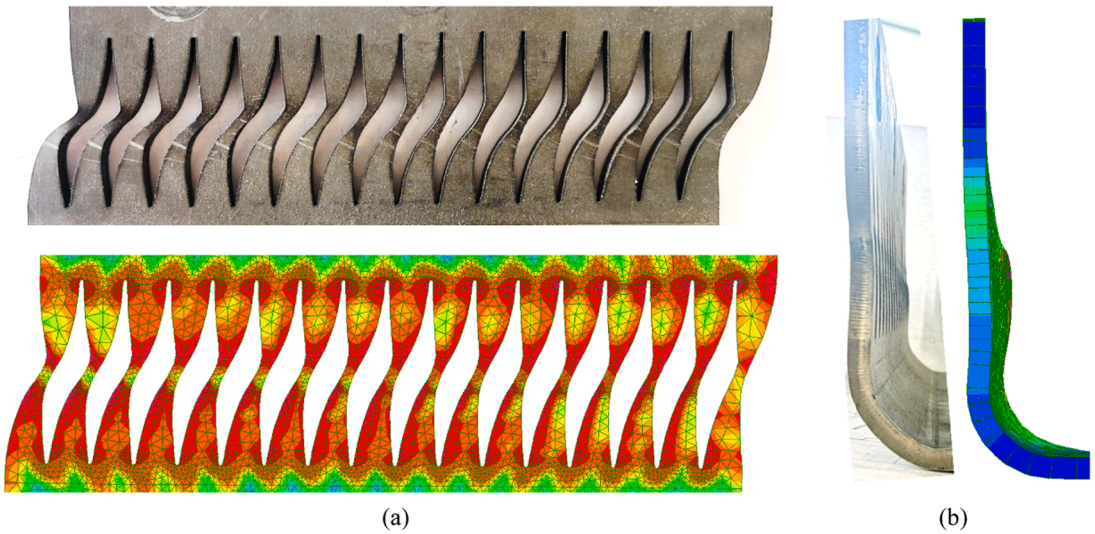

Fig. 13. Comparison of experimental residual deformed shape after test 2 and numerical results: (a) front view, (b) lateral view.

cycles and only few large-displacement cycles are applied to a structure or device. For this experimentation, the following values were considered: $C = 1.3$ *mm;* $A = 1.5$*;* $n = 0…8$*;* $R = 2$ *for test 1 and* $R = 3$ *for test 2.*

$$d_n = C{*}A^n|_{Rx} \tag{1}$$

A different number of cyclic repetitions R was carried out through tests after the evidence in test 1 of a relevant stiffness degradation through cycles, which was not expected for the metallic plate alone. An unexpected millimetric contact between the upper concrete block and the rear base steel plate below the loading jack caused the test to be performed asymmetrically for displacements beyond −6,6 mm in the pull direction for the jack.

During the first cyclic test, a maximum force of 344 kN (172 kN on single MSD angle plate) was achieved at around 29 mm of block relative displacement. The test was interrupted as a consequence of the stroke of the main transducers being exhausted due to the high specimen deformation. Indeed, despite the MSD angle plates were clearly highly plastically deformed (Fig. 11a), failure was not attained.

During the second cyclic test, a maximum force of 463 kN (231 kN on single MSD angle plate) was achieved at the absolute jack displacement of 60 mm. This test was not interrupted after the main transducers exhausted their stroke due to the high specimen deformation, allowing to attain in this case failure. Failure was attained on the side of the grade 8.8 bolted connectors of the MSD angle plate with the lower concrete block, with fracture surface compatible with moderately ductile shear failure. At the maximum load level attained, the mean shear stress on the bottom bolt lines is indeed higher than the nominal shear resistance of the bolts, which explains the observed failure. The MSD angle plates were found clearly highly plastically deformed (Fig. 11b).

In none of the specimens, cracking of the concrete blocks occurred. Concrete local damage was detected in the contact corner close to the loading jack, mainly due to the previously introduced unexpected contact between the top block and the anchor steel plate.

The results of the experimental cyclic tests are plotted in Fig. 12a with reference to the jack instrumentation. They are also plotted with reference to the relative load and displacement of a single MSD angle plate together with the results of the numerical analysis described above in Fig. 12b and in Fig. 12c for test 1 and test 2, respectively. To be noted that the instrument CH5 detached in test 2 prior to the attainment of the ultimate displacement. The simulations carried out considering both restraint conditions are clearly not able to catch the experimental results when analysing the initial steps, where a much larger deformability and a gap effect was found in the test results. This is due to bolt-hole gap tolerances summed to an initial position adjustment involving rigid body motion of the plate in the experimental test, which is not taken into account in the models. Moreover, the shear deformation of the threaded bar connectors also added a contribution. Nevertheless, the simulated stiffness well matches the unloading stiffness of the specimen, confirming the above. The load associated to a clear change of inclination in the experimental tests matched well with the simulated yield load. When analysing the behaviour under larger displacement, it can be noted that the experimental plastic branch has an inclination similar to the simulation considering the restrained condition, whilst the simulation with unrestrained condition provides inaccurate matching. This is expected due to the selected test configuration as described above, and confirms the very remarkable overstrength and post-yielding hardening of the MSD angle plates. Moreover, this is further confirmed when observing the good matching of the curves when plotting the numerical results considering a 5 mm shift, which is deemed to be the order of magnitude of the rigid body motion of the plate, as also observed by the pinching effect and the stiffness degradation through cycles occurred during the experimental hysteresis. The pinching effect might also have been enhanced by local plastic deformation of the plates in correspondence of all the threaded bar connectors, despite no evident bearing stress failure was observed after dismounting the specimens. Concerning the comparison of the displacement capacity, it is evident from both the load and the displacement attained that the experimental deformation resulted much higher than the one predicted by the numerical analysis. This observation leads to the consideration that setting the failure condition even very locally when the ultimate strain is attained in a single finite element of the mesh may be considered as a too severe condition.

The soundness of the comparison between the numerical (restrained condition) and experimental results can also be appreciated when observing the residual plastic deformed shape of one tested plate after Test 2 (Fig. 13a). Similar considerations apply for the out-of-plane deformation trend (Fig. 13b). The lateral view of the displaced shape of the plate shows that moderate out-of-plane deformation and distortion around the bent part of the plate occurred, which caused the stress distribution on the elementary beams to be not fully equal among them. Indeed, the bent part of the plate is not leaned against concrete, and deforms under imposed load or displacement, altering the behaviour of the equivalent flat MSD plate.

The energy dissipation capacity of the tested specimens was evaluated on the basis of the traditional Equivalent Viscous Damping (EVD) approach described in [77] applying the rectangle contour half-quadrant method. Mean EVD curves were evaluated with reference to the relative displacement as the mean among the cycles carried out per each maximum target displacement and maximum load. The data

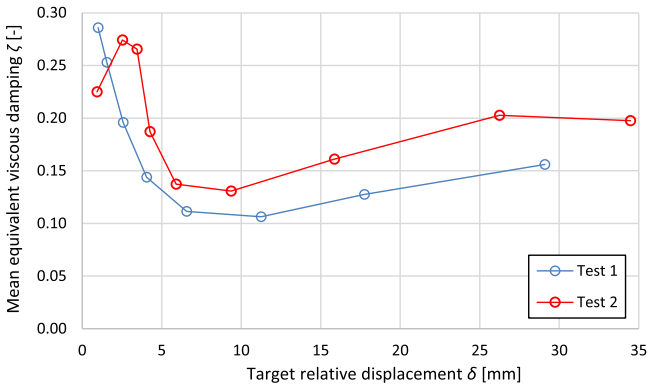

Fig. 14. Mean equivalent viscous damping among experimental cycles.

plotted in Fig. 14 are associated to purely hysteretic energy only (intrinsic viscous damping is assumed null). Due to the asymmetric displacement history applied during both tests, the method was applying evaluating only the energy dissipated in the quadrants of positive displacement, assuming a mirrored behaviour. This assumption becomes progressively less robust with the increase of plastic strain, and therefore the results should be interpreted as indicative. Nevertheless, the following trend is clearly identifiable: an initial branch with high EVD of 0.22–0.28 at very low displacement is most probably due to frictional effects induced by tightening of the connection; the curves rapidly decrease to a minimum of 0.11–0.14; a final increasing branch induced by the strong plasticisation of steel is found with values in between 0.15–0.20. These values are lower with respect to typical maximum EVD attained by hysteretic devices based on plasticisation of steel [11–40], which is due to the cyclic pinching effect described above.

4.1. Parametric analysis

In order to investigate the influence of the angle geometry, and in particular the plate bent area, over the behaviour of MSD angle plates, a parametric analysis was carried out numerically by considering plates having different length (moduli), i.e. the number of elementary beams. Pictures of the 3D models considered with 1, 2, and 3 moduli are shown in Fig. 15.

The results of non-linear static analyses carried out imposing similar conditions of the previously described analyses are shown in the following both in terms of absolute horizontal reaction (Fig. 16) and local normalised reaction of a single elementary beam (Fig. 17). The numerical pushover curves are solid up to the attainment of the ultimate

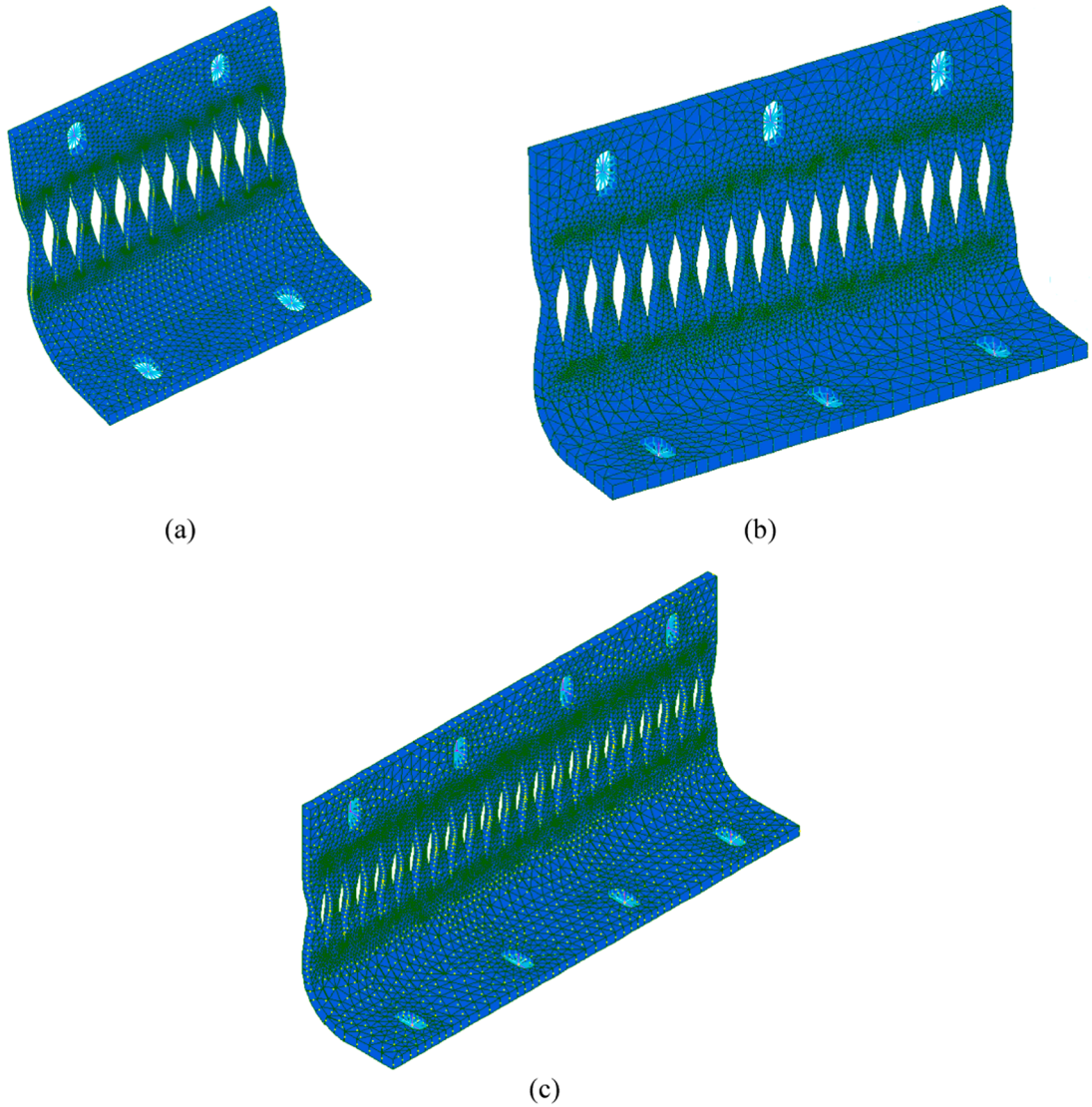

Fig. 15. MSD angular plate with different moduli: (a) 1, (b) 2, (c) 3.

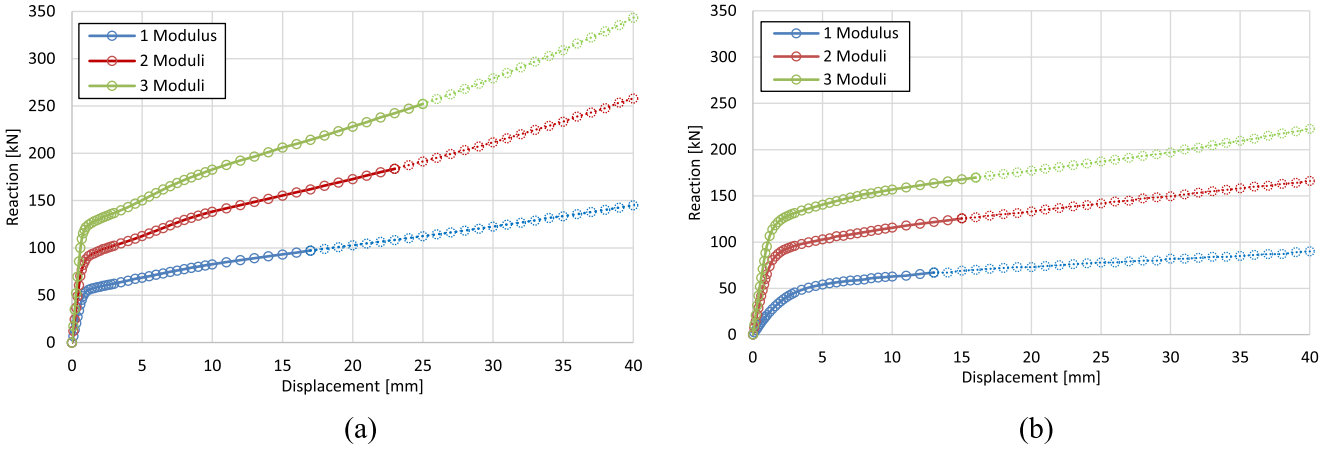

Fig. 16. Results of non-linear static analysis in terms of total reaction vs displacement: (a) restrained condition, (b) unrestrained condition.

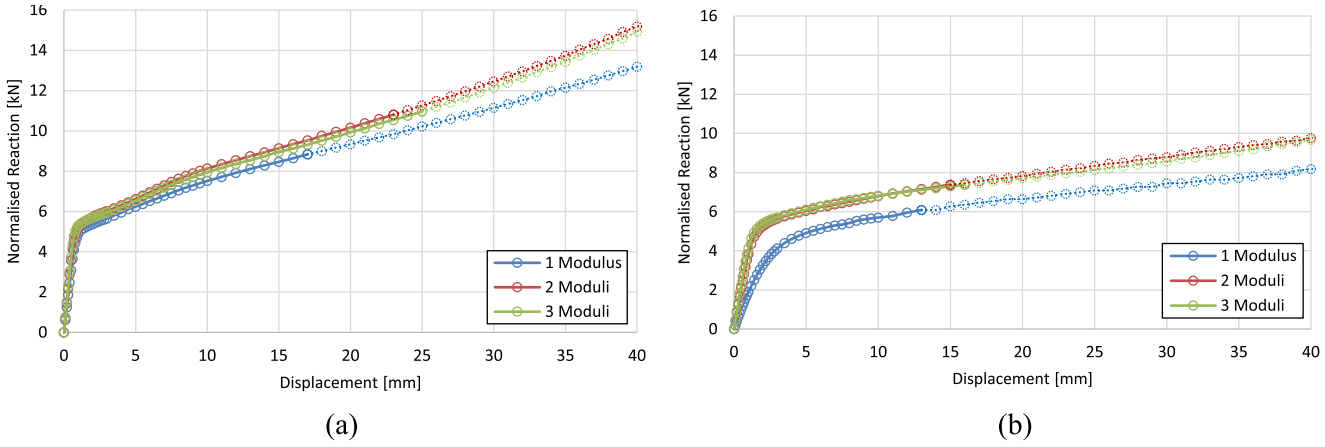

Fig. 17. Results of non-linear static analysis in terms of average reaction of single elementary beam vs displacement: (a) restrained condition, (b) unrestrained condition.

strain, and dashed afterwards. The trends previously highlighted with the plate having 2 moduli are confirmed, with lower initial stiffness, ultimate strength, and ultimate displacement associated to unrestrained condition due to the summation of relevant axial stress to the bending/shear stress imposed by lateral settlement of the plate.

When considering the restrained condition, the displacement associated with the ultimate strain condition slightly increases with the number of moduli, probably due to the limited distortion of longer plates, which turns into lower axial action on the edge elementary beams. Differently, when considering the unrestrained condition, the displacement associated with the ultimate strain changes relevantly with the number of slits, decreasing with it and strongly depending on the number of moduli being odd or even. In particular, relevantly lower ultimate displacement is found with odd numbers of moduli, which is probably due to the higher load acting on the compressed concrete toe due to the lower tension resultant associated with a lower lever arm. This concept will be further analysed and explained in the dedicated chapter about design rules.

The normalised reaction (mean reaction of a single elementary beam) is only moderately affected by the number of moduli for all cases considering restrained conditions and for a number of moduli higher than 1 considering unrestrained condition. A peculiar lower normalised reaction is found for the case with 1 modulus only in the unrestrained condition. This may be explained with the higher influence of the axial component of the stress, which affects a higher percentage of elementary beams, since they are less than the cases with more moduli.

This can also be suggested when looking at the deformed shape of the plates in Fig. 18, which confirms a somehow uniform stress distribution in all elementary beams in the restrained configuration, and a stress concentration due to the axial component in the edge elementary beams with respect to the central, when considering the unrestrained condition (Fig. 19). A larger displacement capacity is shown for the cases with the MSD plates having an odd number of moduli, due to their better capacity to redistribute the axial loading in the elementary beams. On the contrary, the middle elementary beams of the 2-moduli plate result less stressed than the edge ones, since the middle slotted hole is subjected to purely horizontal load, as it will be further analysed and explained in the dedicated chapter about design rules.

4.2. Design rules

A simplified design procedure for the Multiple Slit plate is described in the following. It is recalled that the detailed origin of the proposed design formula of the slitted part of the plate is available in [31]. Considering a single hourglass-profile Timoshenko elementary beam as a double clamped beam subjected to imposed displacement, one can obtain the translational stiffness of the beam as follows, neglecting possible 2nd order effects or combination of axial stress, as per Eq. 2:

$$k_V = 0.43\frac{E \quad b \quad {h_0}^3}{L^3} \tag{2}$$

Leading to a yield displacement as per Eq. 3 equal to:

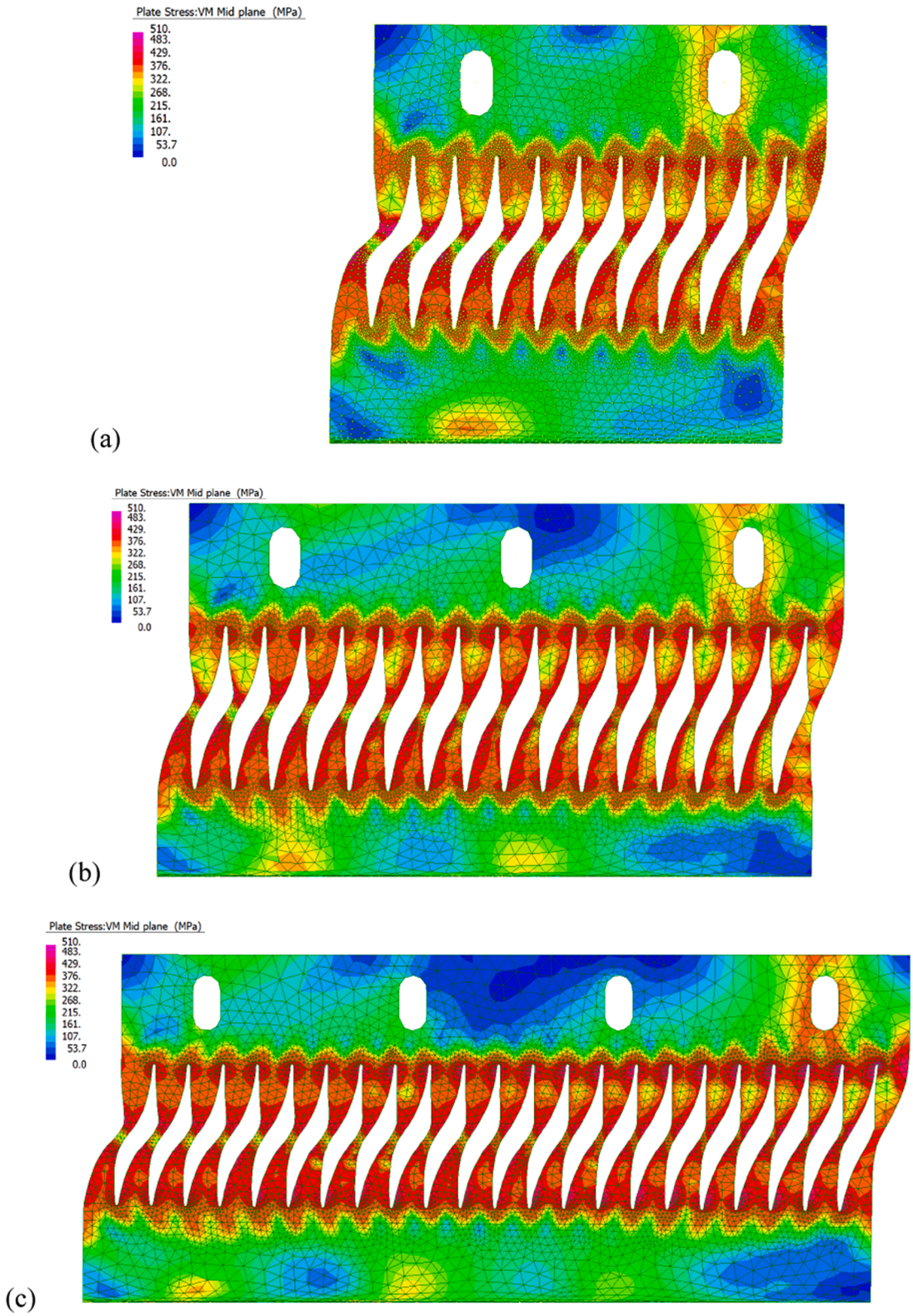

Fig. 18. MSD angular plate with different moduli at attainment of ultimate strain in restrained condition: (a) 1–19 mm, (b) 2–21 mm, (c) 3–26 mm.

$$d_y = 0.78 \quad f_y \frac{L^2}{E \quad h} \tag{3}$$

The corresponding yield load can be obtained by multiplying the yield displacement by the translational stiffness, as per Eq. 4:

$$P_y = k_V \quad d_y \tag{4}$$

The ultimate load is much larger than the first yield load, thanks to the combined effects of diffusion of plasticisation within the cross-section of the elementary beams, and material hardening. The edge chord of the cross section fails when the maximum longitudinal stress reaches the ultimate resistance. All the inner chords, however, are subjected to a lower stress and therefore a contemporaneity factor

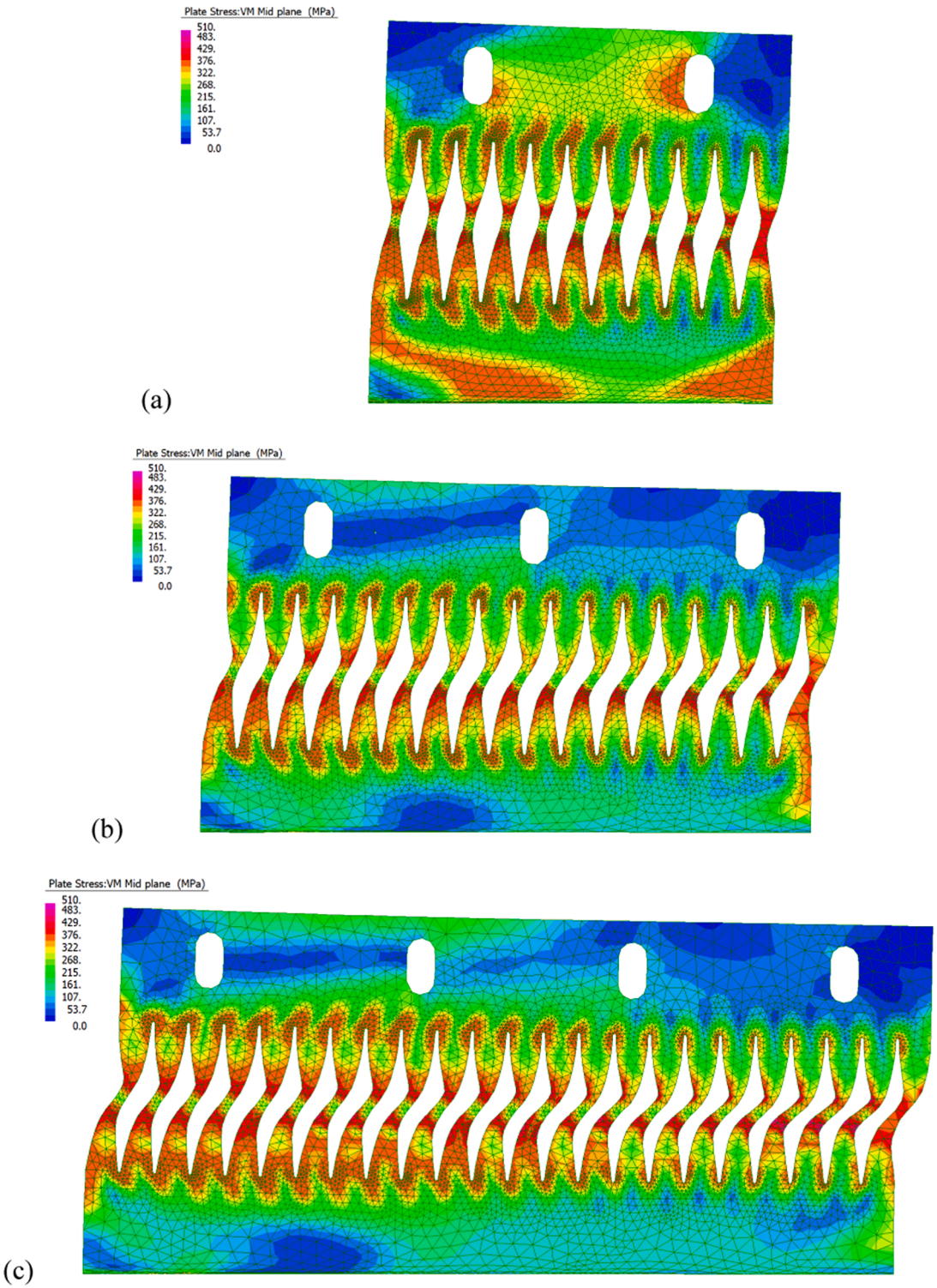

Fig. 19. MSD angular plate with different moduli at attainment of ultimate strain in unrestrained condition: (a) 1–14 mm, (b) 2–8 mm, (c) 3–12 mm.

should be applied to the coefficients referring to those phenomena. Thus, neglecting 2nd order effects which can be done by limiting the base beam height over plate thickness ratio to less than 2 ($h_0 / b \leq 2$), the formulation of the ultimate load can be expressed according to Eq.5:

$$P_u = P_y \quad \varnothing_{pl} \quad \varnothing_{os} \Psi \tag{5}$$

Where Φ_{pl} is the plastic factor of the cross section (being it rectangular, it is equal to 1.50); Φ_{os} is the overstrength factor of steel (being it steel S355, it is equal to 470 / 355 = 1.32); Ψ is the contemporaneity factor which, based on an elastic-parabolic stress-strain relationship of steel, is taken equal to 0.94.

Considering the whole plate, the total yielding or ultimate load can be calculated by multiplying the previously described contribution of the single elementary beam by the total number of elementary beams of the plate. It shall be observed that this formulation neglects the axial stress contribution, which may either strongly or moderately influence the strength of the plate in case of unrestrained or restrained condition, respectively. In fact, this formulation shall not be used if employing the

Table 1
Comparison among analytical, experimental and numerical results for a single plate with restrained condition.

	Analytical						Experimental		Numerical	
	Design strength		Characteristic strength		Mean strength		Test 1	Test 2	FE models	
Moduli	yield	failure	yield	failure	yield	failure	failure	failure	yield	failure
1	48.9	99.4	51.4	104.3	56.5	114.8	-	-	49.0	100.9
2	75.7	153.6	79.4	161.3	87.4	177.4	172.2*	231.7*	81.9	176.5
3	102.3	207.8	107.5	218.2	118.2	240.0	-	-	109.6	257.5

* failure of the plate not fully attained

plate in unrestrained condition, and can be used in restrained condition given the moderate out-of-plane deformation of the plate introduces only moderate axial stress in the edge elementary beams.

The maximum available displacement capacity assumed in design is recommended not to exceed 15.0 % and 8.5 % of the gross length of the elementary beams in case of restrained or unrestrained condition, respectively.

Analytical, experimental, and numerical strengths are compared in Table 1.

Recalling that the numerical results are associated to the nominal material strength, it can be observed that the suggested simplified design procedure correctly tackles the issue, providing safe-sided estimations of the plate strength with respect to both the numerical results and the experimental results. The higher experimental strength may be mainly due to 2nd order effects in tension (catenary effect at large deformations) and to the actual higher plastic deformation capacity and strength of the real steel material employed. A special observation must be done for the plate having 1 modulus only, where the strength is more severely affected by the axial component than the plates with more moduli, for which a higher safety coefficient could be employed (a further strength reduction of 10 % is suggested). Moreover, larger diameter threaded bars should be employed. Nonetheless, this sort of plate is indeed not recommended to be extensively used.

A sketch of the actions on the MSD plate and the bolted connectors is given in Fig. 20, considering both the restrained and unrestrained conditions.

In the restrained condition, the position of the neutral axis of the plate is assumed to be located at midspan of the elementary beams. The plastic shear, mainly arising indeed from the flexural plasticisation of the elementary beam ends, causes bending components to act on both the bolts located at the large flap (as a function of the eccentricity e_1) and at the short flap (as a function of the eccentricity e_2). The bolts located in the large flap, placed orthogonally with respect to the elementary beam axis, are then subjected to combined in-plane shear and out-of-plane shear originated from the torsional equilibrium of the bolted connection system. The bolts located in the short flap, placed parallelly with respect to the elementary beam axis, are then subjected to combined in-plane shear and axial loading, originated from the flexural equilibrium of the bolted connection leaned against concrete. Moreover, the eccentricity e_3 of the shear reactions of large and short flap bolt lines leads to the development of a further out-of-plane bending, which results in an additional out-of-plane shear action on the short flap bolt line.

5. Conclusions

The proposed MSD bolted angle plate may provide an adequate solution for the connection of orthogonal precast walls, with proper stiffness, yield strength, overstrength, ductility, and dissipation capacity.

The numerical simulation of a single plate highlighted this potential, showing for a single proposed MSD angle plate restrained in all directions an elastic stiffness of 120 kN/mm, a yield strength of 87 kN, an ultimate strength of 177 kN (overstrength factor higher than 2), and a displacement capacity of 21 mm.

What referred as the unrestrained MSD angle plate configuration in this paper, meaning a condition which does not restrain the displacement in the direction of the axis of the elementary beams, is discouraged, since it leads to lower strength and much less ductility with respect to the restrained condition, fostering compressive buckling phenomena.

The tests highlighted a very large overstrength factor (failure over yielding) of more than 2.8 due to the combined effects of materials overstrength, plasticity diffusion in the elementary beams, and 2nd order catenary action at large drift. This provides a safe plastic branch with hardening and large stress redistribution potential, but it also shall be carefully taken into account when applying capacity design, e.g. for the design of the bolted connectors.

The tests also showed a marked pinching effect and initial gap due to the combination of bolt-hole gap, rigid position adjustment of the angle plate, shear deformation of the bolted connectors, and bearing stress deformation of the plate, which negatively affected both the stiffness and the hysteretic shape around small displacements. In order to avoid such phenomena to occur, making the real behaviour of the MSD angle plate closer to the ideal behaviour of the numerical simulation, it is suggested to adopt friction bolted connections instead of classical. The issue of tolerances may be dealt by adopting large holes and planetary slotted thick washers.

Moreover, the parametric analysis showed that short MSD angle plates with only few elementary beams are also to be discouraged in favour of longer plates with many elementary beams, since few elementary beams may activate strong local compression and the deformation of the bent angle, thus negatively impacting stiffness and strength of the overall device. Conversely, the deformability of the bent part of the MSD angle plate did not play a remarkable role on the stiffness and strength of longer plates.

The proposed simple design rules were demonstrated by comparison with experimental and numerical tests to be sound and reliable for geometries similar to the proposed.

Careful installation procedures aimed at limiting the pinching effect induced by the above-cited factors are encouraged to be tested before practical applications. Future research may focus on the detailed investigation of the cyclic hysteretic properties of the connection, as well as investigating MSD angle plates with different topology than the one employed in this research.

Declaration of Competing Interest

To the interesting reader, this communication follows the request to preliminary state any potential conflict of interest by any of the authors prior to the submission of a technical paper in the journal Structures.

The writer is partner of DLC Consulting srl of Milan, Italy, which is a Structural Engineering consultant company active in different fields, among which precast concrete structures, the main subject of the paper.

The writer, however, does not see any explicit possible benefit to the financial/commercial activity of the above consultant from the possible dissemination of the paper, also since the content of the paper is not object of patent.

The proposed devices may be used in practical design applications by

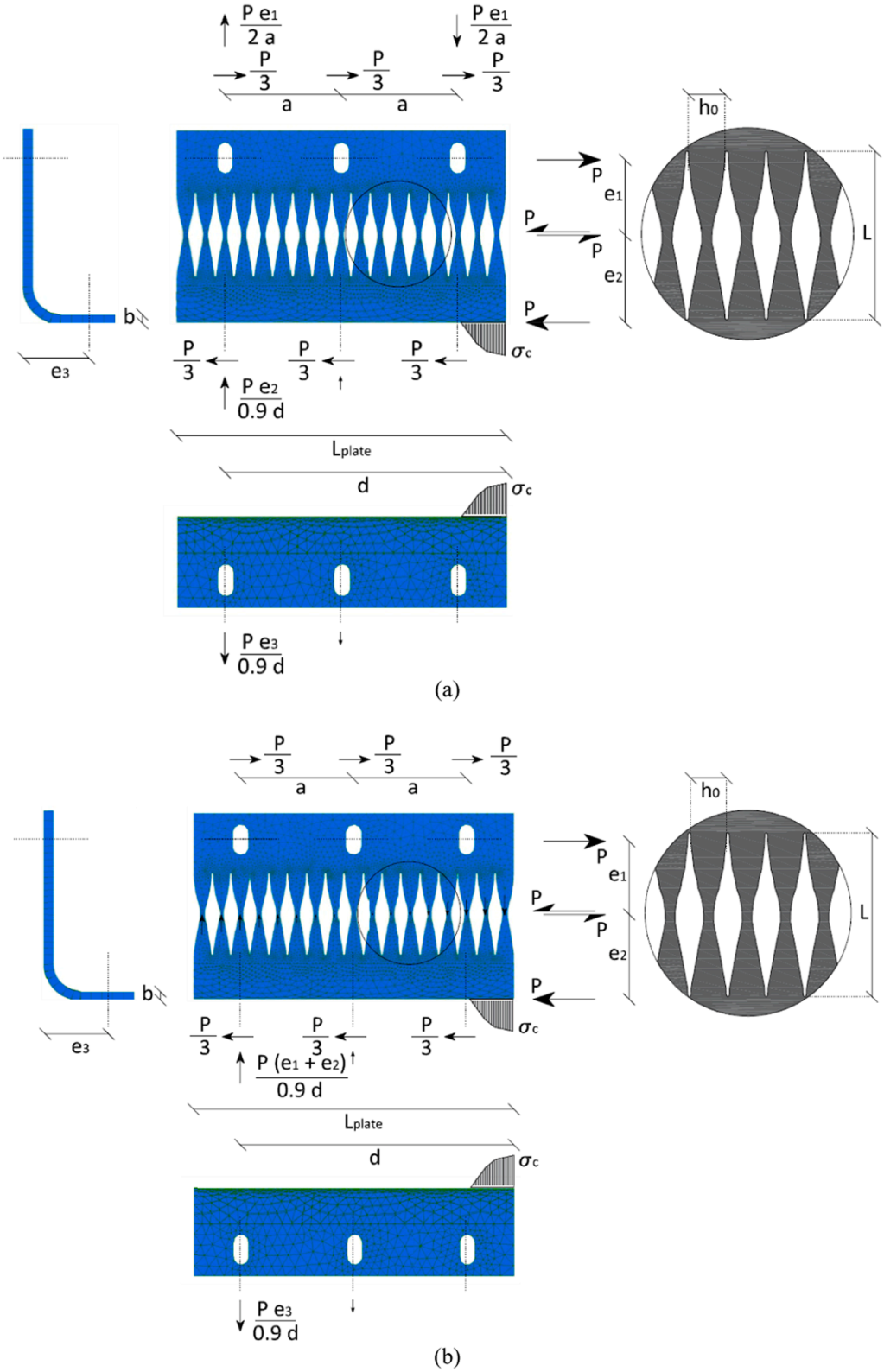

Fig. 20. Design rules for angle Multiple Slit bolted plates: (a) restrained condition; (b) unrestrained condition.

the consultant.

Acknowledgments

The results presented in this paper are part of the results obtained in a comprehensive research project privately financed by DLC Consulting S.r.l. of Milan. The above engineering company received partial funding from the Programme "INNODRIVER S3 - POR FESR 2014–2020" issued by the Italian Region of Lombardy. The company TreColli S.p.a. of Carrosio is acknowledged for the production of the specimens. Krunal Gajera from DLC Consulting s.r.l. of Milan is kindly acknowledged for his contribution in carrying out the numerical analyses; Marco Del Galdo

from DLC Consulting s.r.l. of Milan and Daniele Spinelli from the LPMSC laboratory of Politecnico di Milano are kindly acknowledged for their contribution in experimental testing, partly supervised by Liberato Ferrara and Giovanni Muciaccia from the Department of Civil and Environmental Engineering of Politecnico di Milano.

References

[1] Skinner RI, Kelly JM, Heine AJ. Hysteretic dampers for earthquake-resistant structures. Earthq Eng Struct Dynam 1974;3(3).
[2] Tyler RG. Tapered steel cantilever energy absorbers. Bull N Z Soc Earthq Eng 1978;11(4):282–94.
[3] Whittaker AS, Bertero VV, Thompson CL, Alonso LJ. Seismic testing of steel plate energy dissipation devices. Earthq Spectra 1991;7(4):563–604.
[4] Aiken ID, Nims DK, Whittaker AS, Kelly JM. Testing of passive energy dissipation systems. Earthq Spectra 1993;9(3).
[5] Tsai KC, Chen HW, Hong CP, Su YF. Design of steel triangular plate energy absorbers for seismic-resistant construction. Earthq Spectra 1993;9(3):505–28.
[6] Martínez-Rueda JE. On the evolution of energy dissipation devices for seismic design. Earthq Spectra 2002;18(2):309–46.
[7] Soong TT, Spencer Jr BF. Supplemental energy dissipation: state-of-the-art and state-of-the practice. Eng Struct 2002;24:243–59.
[8] Della Corte G, D'Aniello M, Landolfo R. Field testing of all-steel buckling-restrained braces applied to a damaged reinforced concrete building. ASCE J Struct Eng 2015;141(1):D4014004.
[9] Chesoan IA, Stratan A, Dubina D, Poljansek M, Molina FJ, Ruiz, et al. Experimental validation of re-centring capability of eccentrically braced frames with removable links. Eng Struct 2016;113:335–46.
[10] Fang Q, Sun J, Qiu H, Lago BDal, Chen W. Seismic behavior of precast concrete coupled shear walls with yielding-based and friction-based coupling beams. Arch Civ Mech Eng 2023;23:104.
[11] Garmeh V, Akbarpour A, Adibramezani M, Hojat Kashani A, Adibi M. Introducing and numerical study of an innovative rotational damper with replaceable hourglass steel pins. Struct 2021;33:2019–35.
[12] Zongjing L, Ganping S. Test and evaluation of modified TADAS devices with different grades of steel. Earthq Eng Eng Vib 2020;19:451–64.
[13] Dal Lago B, Del Galdo M, Consiglio A. Soft omega joint for selective weakening of core walls in large precast commercial buildings. Struct 2023;53:949–62.
[14] Hitaka T, Matsui C, Sakai J. Cyclic tests on steel and concrete-filled tube frames with slit walls. Earthq Eng Struct Dyn 2007;36:707–27.
[15] Chan RWK, Albermani F. Experimental study of steel slit damper for passive energy dissipation. Eng Struct 2008;30:1058–66.
[16] Hedayat AA. Prediction of the force displacement capacity boundary of an unbuckled steel slit damper. J Constr Steel Res 2015;114:30–50.
[17] Naeem A, Kim J. Seismic performance evaluation of a multi-slit damper. Eng Struct 2019;189:332–46.
[18] Sun YZ, Li GQ, Sun FF, Jiang J. Experimental study on behavior of steel tube dampers. J Earthq Eng 2019;25(10):2106–26.
[19] Huang W, Hu G, Miao X, Fan Z. Seismic performance analysis of a novel demountable precast concrete beam-column connection with multi-slit devices. J Build Eng 2021;44:102663.
[20] Chen Y, Ye D, Zhang L. Analytical development and experimental investigation of the casting multi-plate damper (CMPD). Eng Struct 2022;250:113402.
[21] Hwang BK, Kim TS, Kim YJ, Kim JW. A comparative study on hysteretic characteristics of austenitic stainless steel and carbon steel slit dampers under cyclic loading. J Build Eng 2022;45:103553.
[22] Oh SH, Park HY. Experimental study on seismic performance of steel slit damper under additional tensile load. J Build Eng 2022;50:104110.
[23] Rousta AM, Gorji Azandariani M, Safaei Ardakani MA, Shoja S. Cyclic behavior of an energy dissipation system with the vertical steel panel flexural-yielding dampers. Struct 2022;45:629–44.
[24] Zhao X, Qi A. Developing and testing innovative beam–column joint damper. Struct 2022;41:1584–601.
[25] Nuzzo I, Losanno D, Caterino N, Serino G, Bozzo Rotondo LM. Experimental and analytical characterization of steel shear links for seismic energy dissipation. Eng Struct 2018;172:405–18.
[26] Nuzzo I, Losanno D, Cilento F, Caterino N. Analytical and numerical modelling of shear-link device for seismic energy dissipation in frame structures. Eng Struct 2020;214:110630.
[27] Ghabraie K, Chan R, Huang X, Xie YM. Shape optimization of metallic yielding devices for passive mitigation of seismic energy. Eng Struct 2010;32:2258–67.
[28] Lee CH, Ju YK, Min JK, Lho SH, Kim SD. Non-uniform steel strip dampers subjected to cyclic loadings. Eng Struct 2015;99:192–204.
[29] Teruna DR, Majid TA, Budiono B. Experimental study of hysteretic steel damper for energy dissipation capacity. Adv Civ Eng 2015;2015:631726.
[30] Köroğlu MA, Köken A, Dere Y. Use of different shaped steel slit dampers in beam to column connections of steel frames under cycling loading. Adv Steel Constr 2018;14(2):251–73.
[31] Dal Lago B, Biondini F, Toniolo G. Experimental tests on multiple-slit devices for precast concrete panels. Eng Struct 2018;167:420–30.
[32] Aminzadeh M, Kazemi HS, Tavakkoli SM. A numerical study on optimum shape of steel slit dampers. Adv Struct Eng 2020;23(14):2967–81.
[33] Bae J, Lee CH, Park M, Alemayehu RW, Ryu J, Kim Y, et al. Cyclic loading performance of radius-cut double coke-shaped strip dampers. Mat 2020;13:3920.
[34] He L, Khadka B. Study on the extended steel plate connection for steel slit shear walls. Struct 2020;28:816–24.
[35] Keykhosro Kiani B, Hosseini Hashemi B, Torabian S. Optimization of slit dampers to improve energy dissipation capacity and low-cycle-fatigue performance. Eng Struct 2020;214:110609.
[36] Mohseni PK, Zahedi-khameneh A, Naeemifar O. Study of the effect of geometric parameters of steel block slit dampers on energy absorption. Int J Steel Struct 2020;20(3):1069–79.
[37] Ahmadi Z, Aghakouchak AA, Mirghaderi SR. Steel slit shear walls with an efficient geometry. Thin Wall Struct 2021;159:107296.
[38] Heyrani Moghaddam S, Shooshtari A. Nonlinear static and dynamic behaviors assessment of self-centering post-tensioned concrete wall with multiple-slit device. J Build Eng 2021;43:102999.
[39] Aljuboori M, Tabatabai H. An energy dissipating seismic connector for precast concrete shear walls. Build 2022;12:949.
[40] Heyrani Moghaddam S, Shooshtari A. Numerical and experimental investigation on seismic performance of proposed steel slit dampers. J Constr Steel Res 2023;200:107646.
[41] Kanyilmaz A. The problematic nature of steel hollow section joint fabrication, and a remedy using laser cutting technology: A review of research, applications, opportunities. Eng Struct 2019;183:1027–48.
[42] Gandelli E, Chernyshov S, Dist J, Dubini P, Weber F, Taras A. Novel adaptive hysteretic damper for enhanced seismic protection of braced buildings. Soil Dyn Earthq Eng 2021;141:106522.
[43] Fazlalipour N, Monir HS, Firouzsalari SE. Circular tube-in-tube dampers for seismic resilience of structures. Adv Struct Eng 2023;26(3):547–63.
[44] Feng S, Tagawa H, Chen X. Seesaw-twisting system with cylindrical steel slit damper for vibration control of structures. Struct 2023;50:1376–90.
[45] Lee CH, Kim J, Kim DH, Ryu J, Ju YK. Numerical and experimental analysis of combined behavior of shear-type friction damper and non-uniform strip damper for multi-level seismic protection. Eng Struct 2016;114:75–92.
[46] Kim J, Shin H. Seismic loss assessment of a structure retrofitted with slit-friction hybrid Dampers. Eng Struct 2017;130:336–50.
[47] Karavasilis TL, Kerawala S, Hale E. Hysteretic model for steel energy dissipation devices and evaluation of a minimal-damage seismic design approach for steel buildings. J Constr Steel Res 2012;70:358–67.
[48] Askariani SS, Garivani S. Introducing and numerical study of a new brace-type slit damper. Struct 2020;27:702–17.
[49] Askariani SS, Garivani S, Aghakouchak AA. Application of slit link beam in eccentrically braced frames. J Constr Steel Res 2020;170:106094.
[50] González-Sanz G, Escolano-Margarit D, Benavent-Climent A. A new stainless-steel tube-in-tube damper for seismic protection of structures. Appl Sci 2020;10:1410.
[51] Guo W, Ma C, Yu Y, Bu D, Zeng C. Performance and optimum design of replaceable steel strips in an innovative metallic damper. Eng Struct 2020;205:110118.
[52] Benavent-Climent A, Escolano-Margarit D, Arcos-Espada J, Ponce-Parra H. New metallic damper with multiphase behavior for seismic protection of structures. Metals 2021;11:183.
[53] Zhai Z, Guo W, Yu Z, Y H, Ma C. Seismic performance assessment of steel strip dampers equipped in high-rise steel frame. J Constr Steel Res 2021;177:106437.
[54] Ellsa Sarassantika IP, Hsu HL. Improving brace member seismic performance with amplified-deformation lever-armed dampers. J Constr Steel Res 2022;192:107221.
[55] Eatherton MR, Hajjar JF, Deierlein GG, Krawinkler H, Billington S, Ma X. Controlled rocking of steel-framed buildings with replaceable energy-dissipating fuses. Proc 14th World Conf Earthq Eng (18WCEE) 2008:12–7.
[56] Ozaki F, Kawai Y, Kanno R, Hanya K. Damage-control systems using replaceable energy-dissipating steel fuses for cold-formed steel structures: seismic behavior by shake table tests. J Struct Eng 2013;139(5):787–95.
[57] Oh SH, Kim YJ, Ryu HS. Seismic performance of steel structures with slit dampers. Eng Struct 2009;31:1997–2008.
[58] Shahri SF, Mousavi SR. Seismic behavior of beam-to-column connections with elliptic slit dampers. Steel Compos Struct 2018;26(3):289–301.
[59] Liu Y, Guo Z, Liu X, Chicchi R, Shahrooz B. An innovative resilient rocking column with replaceable steel slit dampers: experimental program on seismic performance. Eng Struct 2019;183:830–40.
[60] Zhao X, Qi A. Slotted beam-column energy dissipating connections: applicability and seismic behavior. Adv Civ Eng 2021;2021:5530083.
[61] Askariani SS, Garivani S, Hasani M, Hajirasouliha I. Special Truss Moment Frames Equipped with Steel Slit Dampers. Int J Steel Struct 2022;22(1):206–24.
[62] Hosseini M, Haitao L, Corbi I, Corbi O. Numerical analysis of the seismic performance of rigid beam-to-column moment connections equipped with steel slit damper (SSD). Lat Am J Solids Struct 2022;19(2):e436.
[63] Huang W, Hu G, Zhang J. Experimental study on the seismic performance of new precast concrete beam-column joints with replaceable connection. Struct 2022;35:856–72.
[64] Naserpour A, Fathi M, Dhakal RP. Demountable shear wall with rocking boundary columns for precast concrete buildings in high seismic regions. Struct 2022;41:1454–74.
[65] Dal Lago B, Biondini F, Toniolo G. Seismic performance of precast concrete structures with energy dissipating cladding panel connection systems. Struct Conc 2018;19:1908–26.
[66] Zhang H, Li H, Chen X, Li C. Experimental investigation on the hysteretic behavior of precast concrete walls with energy dissipated dry connections. Struct Conc 2020;21:2836–53.
[67] Dal Lago B, Biondini F, Toniolo G. Friction-based dissipative devices for precast concrete panels. Eng Struct 2017;147:356–71.

[68] Fang Q, Qiu H, Sun J, Dal Lago B, Jiang H. Performance study of precast reinforced concrete shear walls with steel columns containing friction-bearing devices. Arch Civ Mech Eng 2021;21(3):110.
[69] Fang Q, Sun J, Qiu H, Jiang H, Dal Lago B, Biondini F. Experimental evaluation on the seismic behavior of precast concrete shear walls with slip-friction devices. J Build Eng 2022;52:104507.
[70] B. Dal Lago, D. Bisi, M. Del Galdo, A. Dal Lago, G. Muciaccia, L. Ferrara, Experimentation and design rules of loop-reinforced diamond-shaped joints for load-bearing precast concrete walls, Italian Concrete Days 2020 (ICD2020), Naples, Italy (2021).
[71] Dal Lago B, Toniolo G, Felicetti R, Lamperti Tornaghi M. End support connection of precast roof elements by bolted steel angles. Struct Concr 2017;18(5):755–67.
[72] Dal Lago B, Biondini F, Toniolo G. Experimental investigation on steel W-shaped folded plate dissipative connectors for precast cladding panels. J Earthq Eng 2018; 22(5):778–800.
[73] Dal Lago B, Del Galdo M, Bisi D. Tests and design of welded-bar angle connections of precast floor elements. J Adv Concr Tech 2022;20(2):43–56.
[74] Jun Y, Sun C, Xu X, Fang Y, Sun B. Experimental study on seismic behavior of a new precast shear wall system with angle steel connectors. Struct 2023;52(1) ():30–41.
[75] G+D Computing. ed. Using Strand7 (Straus7) - Introduction to the Strand7 finite element analysis system, 3. Strand7 Pty Limited; 2010.
[76] EN 1998–1:2004. Eurocode 8: Design of structures for earthquake resistance. Part 1: General rules, seismic actions and rules for buildings. European Committee for Standardization, Brussels.
[77] Dal Lago B, Molina FJ. Assessment of a capacity spectrum design approach against cyclic and seismic experiments on full-scale precast RC structures. Earthq Eng Struct Dyn 2018;47(7):1591–609.